

Applying Miniaturized Atomic Clocks for Improved Kinematic GNSS Single Point Positioning

T. Krawinkel, S. Schön, *Institut für Erdmessung, Leibniz Universität Hannover*

BIOGRAPHIES

Thomas Krawinkel studied “Geodesy and Geoinformatics” at Leibniz Universität Hannover (LUH), and reached his master's degree in October 2012. Subsequently, he became a research assistant at the Institut für Erdmessung (IfE) at LUH. His work mainly focuses on GNSS receiver clock modeling.

Dr. Steffen Schön is professor for positioning and navigation at the IfE, LUH since 2006. Starting in 2003, he has been involved in several GPS projects at DGFI Munich (Germany) and IGMS TU Graz (Austria), especially on landslide monitoring, development of GPS quality indicators, and studies on turbulence theory. His current research interests are the correction and assessment of systematic errors in GNSS, absolute antenna calibration, receiver clock modeling, and improved stochastic models for GNSS observations.

ABSTRACT

Kinematic GNSS (Global Navigation Satellite Systems) single point positioning (SPP) requires epoch-wise estimation of a receiver synchronization error w.r.t. GNSS system time because of the low long-term stability and the generally poor accuracy of the receiver's internal quartz oscillator. Modeling this error source by a linear polynomial instead of epoch-wise estimation improves the precision of the up-coordinate and makes the adjustment more robust.

In this paper we briefly discuss the performance of three different miniaturized atomic frequency standards that were characterized in terms of their frequency stabilities at Physikalisch-Technische Bundesanstalt, Germany. We found significant differences to the manufacturer's data in terms of Allan deviations.

In order to analyze the clock performance when connected to GNSS receivers, a kinematic experiment was carried out with a motor vehicle. Applying miniaturized atomic clocks and properly modeling their behavior in kinematic SPP improves the precision of the up-coordinates by up to 58% and the up-velocities by up to 66%, respectively, compared to epoch-wise receiver clock error estimation. Due to remaining systematic effects the accuracy improvements in the coordinate estimates are distinctly smaller. Furthermore, the impact

of receiver clock modeling on reliability measures in SPP was investigated. We found improvements in internal reliability of up to 16%—depending on the satellite considered—which makes the positioning solution more robust against gross observation errors.

INTRODUCTION

In kinematic GNSS (Global Navigation Satellite Systems) single point positioning (SPP) time synchronization between a receiver's and satellites' time scales is always required. This task is generally accomplished by aligning these two time scales to GPS time by means of so called clock errors. On the satellite side this is realized by applying clock corrections transmitted by the GNSS system provider, e.g. via broadcast ephemeris, or diverse clock and orbit products of the International GNSS Service (IGS) [1]. Due to the limited long-term (>1 s) frequency stability of the receiver's internal quartz oscillator and its generally poor accuracy the receiver clock error has to be estimated epoch-by-epoch together with other parameters, e.g. the coordinates. This approach itself is uncritical. However, some consequences are (i) very high mathematical correlations of 83% to 99% [2]—depending on the elevation cutoff angle applied—between the height component and the clock parameters, and other elevation-dependent error sources, and (ii) the height coordinate is typically determined two to three times worse than the horizontal coordinates.

This situation can be dramatically improved when connecting GNSS receivers to more stable clocks and modeling their behavior in a physically meaningful way instead of epoch-wise estimating clock errors. Additionally, positioning is still possible with only three satellites in view, thereby increasing availability and continuity because of one unknown parameter less to be estimated. Hence, the geometry of GNSS positioning (hyperbolic navigation) gets closer to a true trilateration problem. Especially kinematic positioning benefits from such an approach called receiver clock modeling (RCM) [3].

Recent developments of low-priced and low power consuming miniaturized atomic clocks (MACs), primarily Chip Scale Atomic Clocks (CSACs), allow for usage in kinematic GNSS applications. Thus, replacing the internal oscillator by one of these much more stable external frequency standards opens up the possibility of RCM.

The most important requirement for this approach is that the receiver clock noise has to be below the noise of the GNSS observations in use—typically assumed to be one percent of the signal's wavelength—over a certain time span in which RCM shall be applied.

In this paper, first, we investigate the performance of three different MACs—namely *Jackson Labs LN CSAC*, *Symmetricon SA.45s CSAC*, and *Stanford Research Systems PRS10*—in terms of their frequency stability. The resulting Allan deviations (ADEV) [4] are used for RCM in GNSS data analysis to adequately model the stochastic behavior of the abovementioned atomic clocks.

Subsequently, we describe and examine the results of a kinematic experiment and show the performance improvements of RCM in kinematic SPP.

CHARACTERIZATION OF FREQUENCY STABILITY

Clock comparisons at Physikalisch-Technische Bundesanstalt

In order to correctly model the behavior of any frequency standard its frequency stability has to be known. Generally, this information is provided by the manufacturer in terms of ADEV values for certain averaging times. However, the given ADEV are often only available for few averaging times and they are not instrument specific but for a whole product series. This is also true for the present case study, hence, individual clock characterizations are assumed to be necessary to fully exploit the capabilities of the MACs and model their stability correctly.

The stability of a frequency standard can be determined by comparison with a frequency standard of at least one order of magnitude higher stability. To this end, an extensive measurement campaign was carried out in December 2013 and January 2014 at Physikalisch-Technische Bundesanstalt (PTB)—Germany's national metrology institute. The clocks' 10 MHz output signals were compared to the phase of an active hydrogen maser (*VREMYA-CH VCH-1003A*) by means of a multi channel phase comparator (*TimeTech GmbH*) with a selectable sampling interval of 1 s or 100 s. The 1 s measurements were carried out several times for a couple of hours and the 100 s measurements for more than a week, respectively, thus enabling optimal determination of the short- and long-term stabilities of the devices under test.

At this point it is important to note that the Jackson Labs instrument provides two different output signals: one generated by its main CSAC module and another generated by an OCXO (Oven Controlled Crystal Oscillator) post-filter which is steered to the CSAC module generating an output signal with increased short-term stability w.r.t. the CSAC output signal. Consequently, from here on we will distinguish this particular device into two separate oscillator types, namely *Jackson Labs CSAC* and *Jackson Labs OCXO*.

Raw Data Analyses

After removing a deterministic frequency offset and drift the corresponding ADEV are computed. The analyses of raw frequency data enable some insights into the clocks' principal stability. The main findings are:

- The Jackson Labs instrument shows a minimal frequency offset and drift of 1E-11 and 1E-12 per day, respectively. The frequency deviations amount to $\pm 2\text{E-}10$ for the CSAC module, and $\pm 2\text{E-}11$ for the OCXO post-filter, thus, the latter is ten times less noisy than the CSAC module.
- The Symmetricon CSAC performs comparable to the Jackson Labs CSAC in terms of frequency offsets while we detected a strong long-term drift of about 5E-11/day. The overall noise of the fractional frequency data is half as large as the Jackson Labs' CSAC.
- The SRS PRS10 shows a frequency offset of approximately 1E-12 and a long-term drift of 1E-12/day. After removing these deterministic effects the frequency deviations amount to $\pm 2\text{E-}12$.

For more details on the clock comparisons the reader is referred to [5].

Allan Deviations

In order to characterize short- and long-term stability of the investigated instruments, and the predominant noise processes, the overlapping ADEV (O-ADEV) are computed which are most commonly used in frequency stability analysis due to the increased statistical confidence of its estimates [6]:

$$\sigma_y^2(\tau) = \frac{1}{2m^2(M-2m+1)} \cdot \sum_{j=1}^{M-2m+1} \left(\sum_{i=j}^{j+m-1} y_{i+m} - y_i \right)^2, \quad (1)$$

where y_i is the i -th of M fractional frequency values averaged over the sampling interval τ with averaging factor m . Note that (1) denotes the Allan variance which can be easily converted to ADEV by taking its square root. Four different noise types are detectable in the ADEV results, cf. Tab. 1. A qualitative assessment of the dominant power law noise process is possible by the characteristic slope α of the ADEV in a log-log plot.

Tab. 1: Noise types of atomic clocks under test.

Noise type	Abbreviation	α
White noise phase modulation	WPM	2
White noise frequency modulation	WFM	0
Flicker noise frequency modulation	FFM	-1
Random walk frequency modulation	RFM	-2

Fig. 1 shows the resulting O-ADEV values for averaging times from one second to approximately one day. For comparison reasons the manufacturer's values are depicted in Fig. 2. The Jackson Labs CSAC exhibits WFM up to approx. one hour—being about 1.5 times worse than manufacturer's data indicate—, and then transitions into FFM. The OCXO post-filter shows high

short-term stability which is typical for an oscillator type like this. Its overall performance is comparable to the manufacturer's data. Furthermore, steering and adjusting to the CSAC module after approx. half an hour (1800 s) is clearly visible since the dominant noise process changes at the bump in the corresponding O-ADEV curve at that (averaging) time.

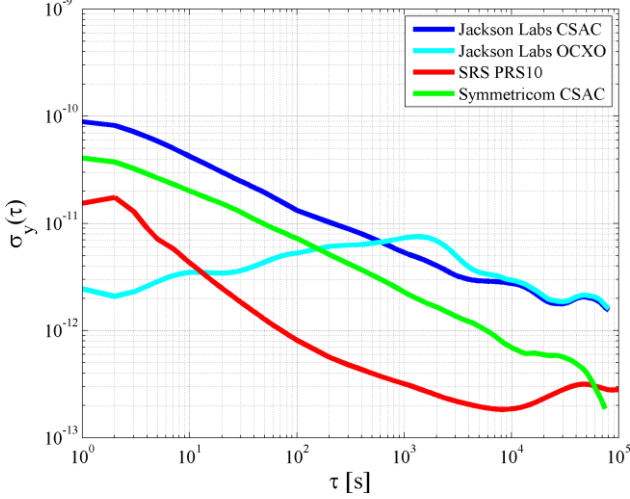


Fig. 1: Overlapping Allan deviations of atomic clocks under test.

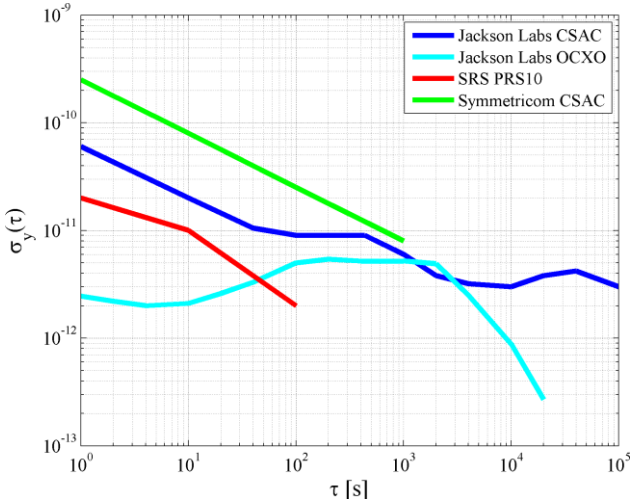


Fig. 2: Allan deviations derived from manufacturer's data.

The Symmetricom CSAC shows similar noise types to the Jackson Labs' CSAC, but the WFM is about $5E-11$ smaller. The flicker floor (FFM) begins after roughly three hours. We found that the performance of our instrument is more than five times better than specified by the manufacturer (cf. Fig. 1 and Fig. 2).

The SRS PRS10 exhibits fluent passages of four different noise types starting with WPM up to approx. 15–20 s, and then transitioning into WFM. A short period of FFM around $\tau=2$ hours is followed by RFM. Due to the fact that only few manufacturer's values are available it can only be stated that our calculated values agree well with the short-term stability shown in Fig. 2.

Derivation of Power Spectral Density Coefficients

In order to use these results as adequate input data for receiver clock modeling in GNSS SPP by extended

Kalman Filtering (EKF), the computed ADEV have to be converted to power spectral density (PSD) coefficients. In our case study we use the so called h_a -coefficients [7]:

$$\begin{aligned} h_2 &= \sigma_y^2(\tau) \cdot \frac{4\pi^2\tau^2}{3f_h}, \\ h_0 &= \sigma_y^2(\tau) \cdot 2\tau, \\ h_{-1} &= \frac{\sigma_y^2(\tau)}{2 \ln 2}, \\ h_{-2} &= \sigma_y^2(\tau) \cdot \frac{3}{2\pi^2\tau}, \end{aligned} \quad (2)$$

where the ADEV are taken from Fig. 1, and f_h denotes the measurement bandwidth of 10 MHz. The resulting numerical values are listed in Tab. 2 and shown in Fig. 3. For further details we refer to [5].

Tab. 2: Spectral density coefficients of atomic clocks under test, derived from Allan deviations.

Oscillator type	h_2	h_0	h_{-1}	h_{-2}
Jackson Labs CSAC	–	3.6E-20	6.5E-24	–
Jackson Labs OCXO	–	–	4.2E-24	1.5E-26
SRS PRS10	3.5E-28	1.4E-22	2.3E-26	3.3E-31
Symmetricom CSAC	–	7.2E-21	2.6E-25	–

KINEMATIC GNSS SINGLE POINT POSITIONING

Concept of Receiver Clock Modeling

Besides the computed h_a -coefficients Fig. 3 also shows GPS code and carrier noise, derived from the observation noise of code and phase observations. We assumed 1 m for C/A-Code, 0.3 m for ionosphere-free P-Code (P3), and 5 mm for ionosphere-free phase (L3) observations, respectively. Taking an elevation-dependent weighting in GNSS data analysis and minimal TDOP for mid-latitudes [3], the observation noise is mapped onto the parameter domain (here: the clock). These values are then modeled as WPM over time.

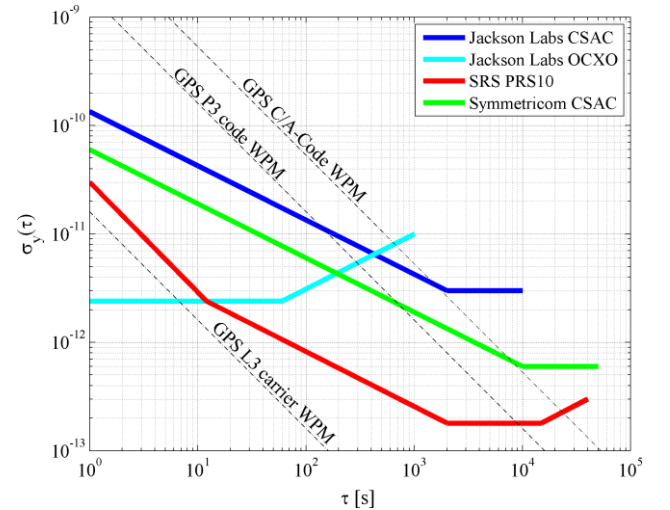


Fig. 3: PSD coefficients derived from ADEV. The dashed lines indicate GPS code and carrier WPM (C/A: 1.6 m; P3 code iono-free: 0.5 m; L3 phase iono-free: 5 mm). Intersection points with ADEV curves indicate maximal time intervals for physically meaningful RCM.

Hence, the intersection points between those dashed GPS noise lines and the ADEV curves define maximal time

intervals for physically meaningful RCM for each MAC. Within these intervals the MACs' noises are below the GNSS observation noise. Thus, the clocks' random phase and frequency fluctuations cannot be resolved by the respective GNSS observation type. Obviously, in our case study, all MACs are well suited for code-based RCM over time intervals of 100–8000 s for P3 and 800–20000 s for C/A-Code observations, respectively.

Experiment

In order to examine the performance of the MACs in real kinematic GNSS SPP applications an experiment was carried out on April 29, 2014, consisting of several test drives on a cart-road in the vicinity of Hannover. Every drive lasted approx. 8–10 minutes and was performed in an eight-shaped manner so that all possible directions and all possible changes of direction were included in the recorded observation data. The chosen area is a best case scenario because of little obstructions along the track. Only an alley in the southern part caused some signal discontinuities and shadowing effects (Fig. 4).



Fig. 4: Test track area of kinematic experiment with an expansion of ca. 500 x 800 m² (Source: Google Earth).

The measurement configuration was a zero-baseline configuration consisting of five *JAVAD Delta TRE-G3T(H)* receivers of basically the same type run by the same firmware version (3.4.14), and connected to the same antenna (*NovAtel 703 GGG*) via an active signal splitter.

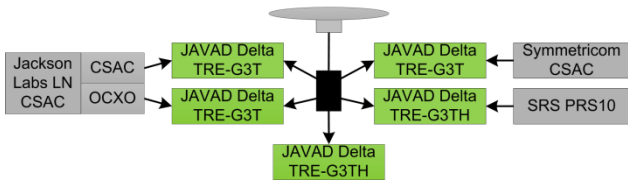


Fig. 5: Measurement configuration of kinematic experiment.

Four of these receivers were connected to the aforementioned MACs, and one driven by its internal quartz oscillator (cf. Fig. 5). We recorded dual-frequency GPS and GLONASS observation data with a sampling interval of 1 s. Additionally, a local reference station was

installed for the time of the experiment, consisting of a *Leica AX1202 GG* antenna and a *Leica GRX1200+ GNSS* receiver, recording GNSS data in the same way as the five mobile receivers.

Data analysis

Analyzing the impact of RCM on coordinate and velocity estimation in terms of precision and accuracy requires a reference solution (for every test drive made). To this end, in a first step a GPS+GLONASS precise point positioning (PPP) [8] solution is computed for the local reference station with *Bernese GNSS Software 5.2* [9]. We use the following mandatory external data sets:

- final satellite orbit and clock solutions from European Space Operations Centre (ESOC),
- satellite specific differential code biases (DCBs) from Center for Orbit Determination in Europe (CODE),
- Vienna Mapping Function 1 (VMF1) coefficients for tropospheric modeling [10]
- atmospheric and ocean tide loading coefficients from [11] and [12], respectively.

The whole data processing contains about two hours of observation data, yielding geocentric coordinates accurate to a few centimeters.

Subsequently, these coordinates are held fixed as geodetic datum in the relative analysis of the five mobile receivers w.r.t. the local reference station. For this purpose we use NovAtel's software package *Waypoint 8.50* calculating ECEF (Earth-Centered, Earth-Fixed) coordinates and velocities for each mobile receiver based on phase and phase-based Doppler observations, respectively. Finally, for each test drive, the five single solutions are combined into one weighted mean solution serving as reference for the code-based solutions.

The actual code-based SPP analysis w/o and w/RCM is performed with our *IfE GNSS MATLAB Toolbox* by means of an forward EKF. In order to generate a typical single-frequency user PVT (Position, Velocity, and Time) solution we only use GPS C/A-Code and L1 Doppler observations, broadcast ephemeris, and models by Saastamoinen and Klobuchar to account for tropospheric and ionospheric signal delays, respectively.

Herein, receiver clock modeling is applied by the model proposed by [13]—considering WFM, FFM, and RFM—using the h_a -coefficients listed in Tab. 2. The corresponding EKF process noise matrix for the two clock states (offset and drift) reads

$$Q_{\omega\omega} = \begin{bmatrix} q_{11} & q_{12} \\ q_{21} & q_{22} \end{bmatrix} \quad (3)$$

with

$$q_{11} = \frac{h_2}{2} \Delta t + 2h_{-1} \Delta t^2 + \frac{2}{3} \pi^2 h_{-2} \Delta t^3,$$

$$q_{12} = q_{21} = h_{-1} \Delta t + \pi^2 h_{-2} \Delta t^2,$$

$$q_{22} = \frac{h_0}{2\Delta t} + 4h_{-1} + \frac{8}{3} \pi^2 h_{-2} \Delta t,$$

where Δt denotes the clock modeling time interval.

Coordinate Results w/o Receiver Clock Modeling

Exemplarily, the SPP analysis is carried out for the third drive of the experiment. Firstly, the coordinate results with and without receiver clock modeling are discussed, followed by the same procedure for the velocity results.

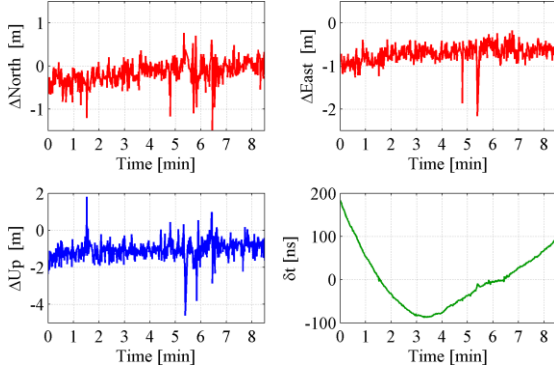


Fig. 6: Internal oscillator—topocentric coordinates w.r.t. reference solution and *non-modeled* receiver clock time offset after straight line fit.

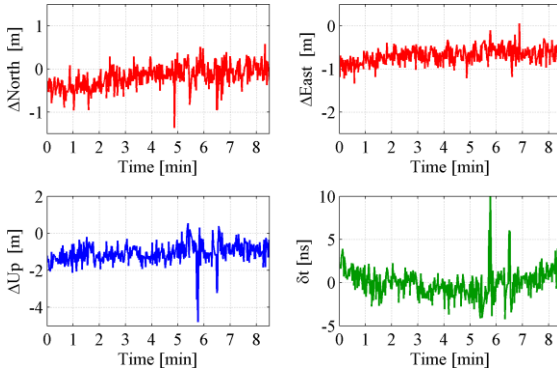


Fig. 7: Jackson Labs OCXO—topocentric coordinates w.r.t. reference solution and *non-modeled* receiver clock time offset after straight line fit.

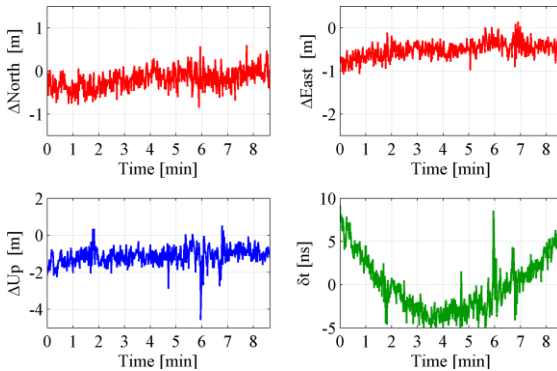


Fig. 8: Jackson Labs CSAC—topocentric coordinates w.r.t. reference solution and *non-modeled* receiver clock time offset after straight line fit.

Fig. 6–10 show topocentric coordinate time series of every involved receiver (cf. Fig. 5) w.r.t. the reference solution. At first glance, offsets can be seen in all coordinate components. On the one hand this is due to different orbit types (IGS vs. broadcast) applied in data analysis. On the other hand these offsets are mainly caused by remaining ionospheric effects. When applying IONEX TEC maps [14] or the ionosphere-free linear

combination to the P-Code observations the coordinate offsets are eliminated almost completely. The overall noise in the coordinate time series is in the range of one to two meters which is typical for code-based positioning with geodetic GNSS receivers.

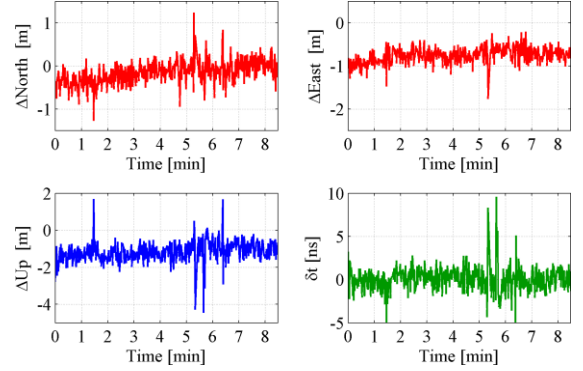


Fig. 9: SRS PRS10—topocentric coordinates w.r.t. reference solution and *non-modeled* receiver clock time offset after straight line fit.

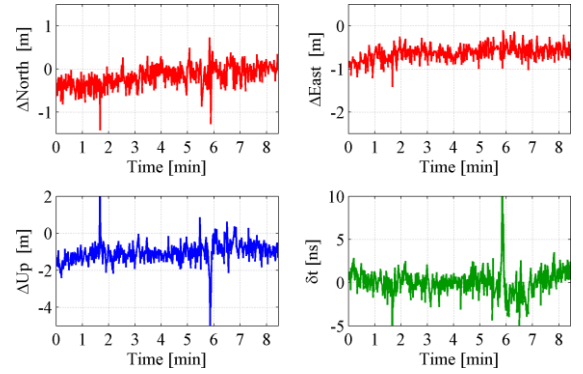


Fig. 10: Symmetricom CSAC—topocentric coordinates w.r.t. reference solution and *non-modeled* receiver clock time offset after straight line fit.

Unsurprisingly, the (residual) clock estimates of the receiver driven by its internal oscillator (Fig. 6) reflect the much lower accuracy and stability of the inbuilt quartz. In contrast, the clock error estimates of each receiver connected to an external clock range homogeneously between -5 and $+10$ nanoseconds. For the approx. eight minute lasting test drive the behavior of the MACs is pretty much the same, although, the Jackson Labs device exhibits a certain quadratic systematic.

Furthermore, in this four cases (Fig. 7–10), the typical high correlations between up-coordinate and clock estimates are clearly visible, especially from minutes five to seven when driving through the aforementioned alley causing signal discontinuities and shadowing. These effects also cause increased deviations of the North and East components from the reference solution.

Coordinate Results with Receiver Clock Modeling

Applying the clock noise model defined in (1) combined with the h_a -coefficients of Tab. 2 yields the topocentric coordinate time series depicted in Fig. 11–14. Compared to the results w/o RCM in the previous section no impact on the horizontal coordinates are detectable. However, the up-coordinate and the clock error time series are

smoothed drastically. The high-frequency noise (differences to the mean value) is reduced for each receiver connected to a MAC. This leads to increased precision (decreased standard deviation) of the height estimates between 46% and 55% (Tab. 3)—dependent on the clock in use—w.r.t. SPP w/o RCM (Fig. 7–10). Furthermore, systematic spikes are eliminated, e.g. around minutes two and six (cf. Fig. 10 and Fig. 14).

The accuracy increase is not so strong than that in precision due to the aforementioned remaining systematic (ionospheric) effects. The RMSE (root mean square error) of the up-coordinate time series is reduced by 8% to 15% depending on the MAC in use.

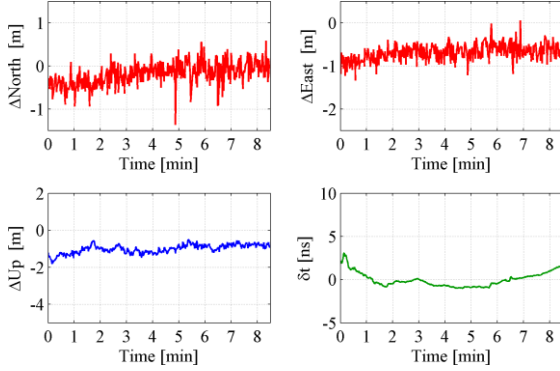


Fig. 11: Jackson Labs OCXO—topocentric coordinates w.r.t. reference solution and *modeled* receiver clock time offset after straight line fit.

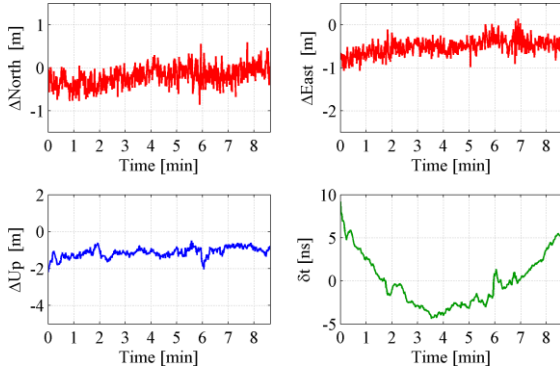


Fig. 12: Jackson Labs CSAC—topocentric coordinates w.r.t. reference solution and *modeled* receiver clock time offset after straight line fit.

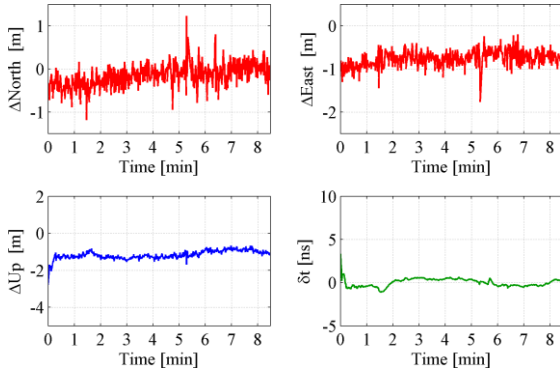


Fig. 13: SRS PRS10—topocentric coordinates w.r.t. reference solution and *modeled* receiver clock time offset after straight line fit.

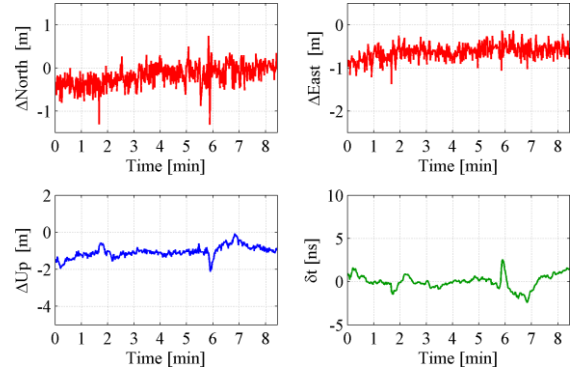


Fig. 14: Symmetric CSAC—topocentric coordinates w.r.t. reference solution and *modeled* receiver clock time offset after straight line fit.

Tab. 3: Improvements in up-coordinate residuals (STD: standard deviation; RMSE: root mean square error).

	JL OCXO	JL CSAC	SRS PRS10	Symm. CSAC
STD w/o RCM [m]	0.52	0.49	0.54	0.58
STD w/RCM [m]	0.23	0.26	0.23	0.31
Improvement [%]	55	46	58	47
RMSE w/o RCM [m]	1.22	1.26	1.31	1.23
RMSE w/RCM [m]	1.04	1.16	1.19	1.11
Improvement [%]	15	8	9	10

Velocity Results w/o Receiver Clock Modeling

Due to the additional processing of Doppler observations also receiver velocities can be estimated, thereby giving direct access to the frequency offset of the receiver's oscillator or the MAC if connected, respectively.

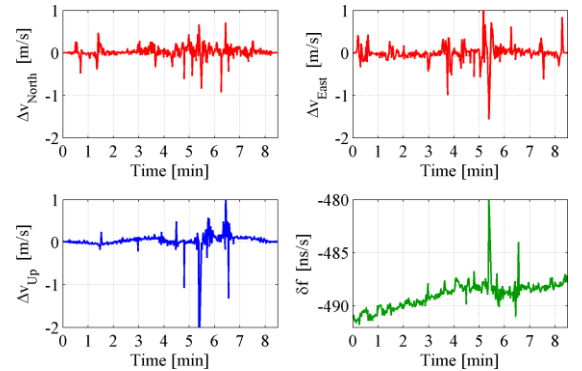


Fig. 15: Internal oscillator—topocentric velocities w.r.t. reference solution and *non-modeled* receiver clock frequency offset.

Similarly to the previous two sections, at first, the resulting topocentric velocity time series of each involved receiver w.r.t. the reference solution shown in Fig. 15–19 are examined, and then compared to the solutions with receiver clock modeling (Fig. 20–23). In principle, the SPP velocities show good agreement with the reference solution with mean scattering of 0.1 m/s. The highest deviations of up to 2 m are found from minute 5 to 7 when driving through the alley which can be seen especially in case of the receiver driven by its internal oscillator. A frequency drift typical for a quartz oscillator can also be seen (cf. Fig. 15). In contrast to the coordinate results the spikes around minutes 5 to 7 are reduced just because the receivers are connected to a MAC.

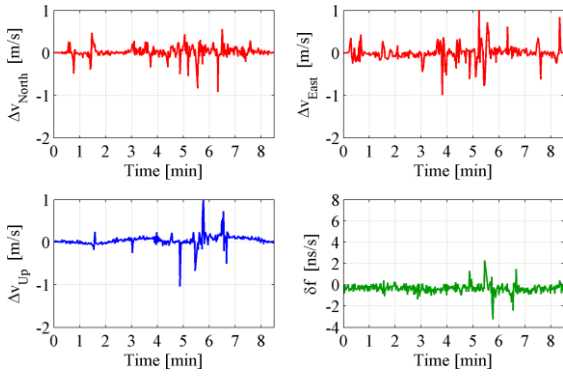


Fig. 16: Jackson Labs OCXO—topocentric velocities w.r.t. reference solution and *non-modeled* receiver clock frequency offset.

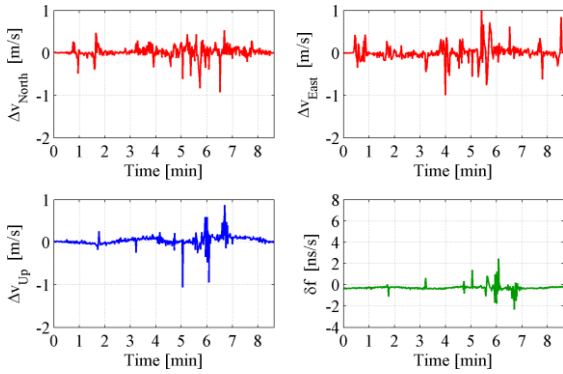


Fig. 17: Jackson Labs CSAC—topocentric velocities w.r.t. reference solution and *non-modeled* receiver clock frequency offset.

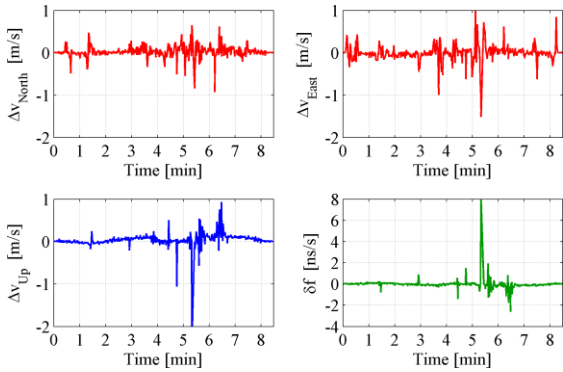


Fig. 18: SRS PRS10—topocentric velocities w.r.t. reference solution and *non-modeled* receiver clock frequency offset.

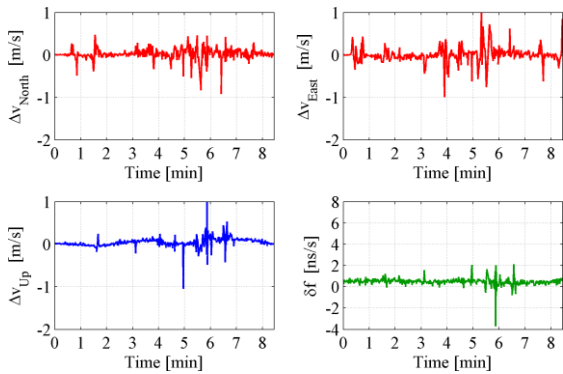


Fig. 19: Symmetricom CSAC—topocentric velocities w.r.t. reference solution and *non-modeled* receiver clock frequency offset.

Velocity Results with Receiver Clock Modeling

When applying RCM, again, the noise in the up-component/velocity and the frequency offset time series is mainly reduced. This leads to an increased precision of the up-velocities in the range of 40% to 66% depending on the MAC in use. Due to the fact that the differences between SPP and reference solution scatter around zero mean the accuracy improvements amount to almost the same values (cf. Tab. 4).

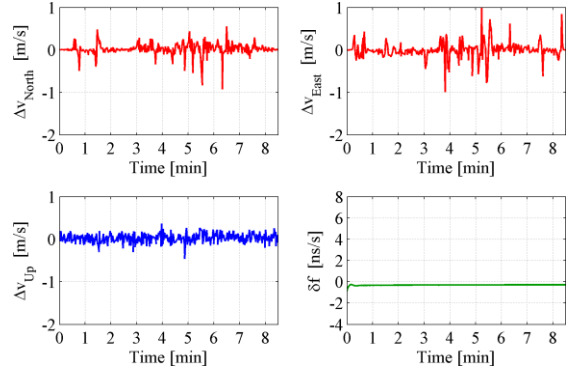


Fig. 20: Jackson Labs OCXO—topocentric velocities w.r.t. reference solution and *modeled* receiver clock frequency offset.

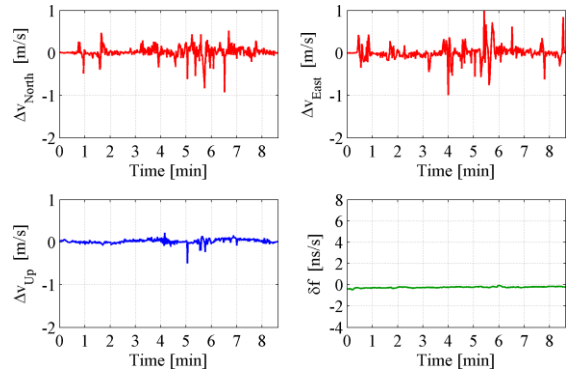


Fig. 21: Jackson Labs CSAC—topocentric velocities w.r.t. reference solution and *modeled* receiver clock frequency offset.

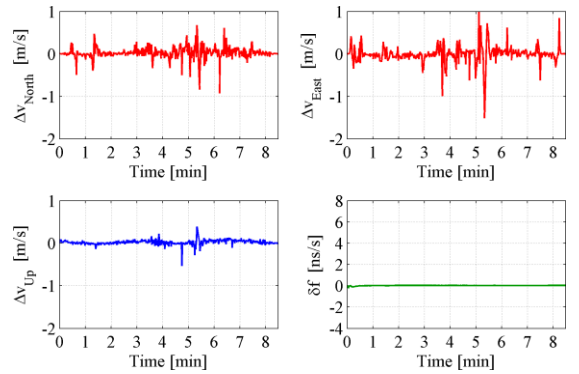


Fig. 22: SRS PRS10—topocentric velocities w.r.t. reference solution and *modeled* receiver clock frequency offset.

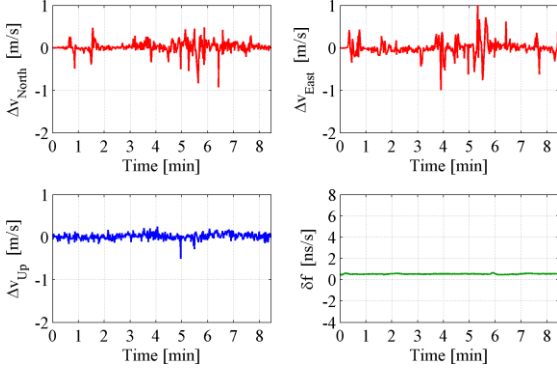


Fig. 23: Symmetricom CSAC—topocentric velocities w.r.t. reference solution and *modeled* receiver clock frequency offset.

Tab. 4: Improvements in up-velocity residuals (STD: standard deviation; RMSE: root mean square error).

	JL OCXO	JL CSAC	SRS PRS10	Symm. CSAC
STD w/o RCM [m/s]	0.12	0.12	0.16	0.12
STD w/RCM [m/s]	0.06	0.05	0.05	0.07
Improvement [%]	53	57	66	40
RMSE w/o RCM [m/s]	0.13	0.13	0.17	0.13
RMSE w/RCM [m/s]	0.06	0.03	0.06	0.07
Improvement [%]	55	55	65	41

Reliability

Besides precision and accuracy, reliability is a key performance parameter in (GNSS) navigation applications. We distinguish between *internal* and *external* reliability which can both be calculated without any actual measurements. Internal reliability a.k.a. *minimal detectable bias* (MDB) refers to which extent a gross measurement error can be detected during outlier detection. On the other hand, external reliability measures the impact of an undetectable gross error on the resulting parameters, e.g. coordinates, and is thus a direct consequence of internal reliability [15].

In an EKF the MDB values for the i -th observation $\nabla \mathbf{z}_i$ at a given epoch can be computed from the current covariance-covariance matrix \mathbf{Q}_{dd} of the innovation vector \mathbf{d} , and the non-centrality parameter λ which depends on the chosen test quality and probability of error, in this case study 80% and 1%, respectively:

$$\nabla \mathbf{z}_i = \sqrt{\frac{\lambda}{(\mathbf{Q}_{dd}^{-1})_{ii}}}. \quad (4)$$

Each of these MDB values has a different impact on the parameter vector \mathbf{x} . Considering the Kalman gain matrix \mathbf{K} yields the external reliability caused by the MDBs:

$$\nabla \mathbf{x}_i = \mathbf{K} \nabla \mathbf{z}_i. \quad (5)$$

MDB values can be computed for every satellite in view. Fig. 24 and Fig. 25 depict these values for the whole observation time of the third test drive w/o and with receiver clock modeling, respectively. Additionally, the minimal and maximal MDB improvements of 0.1% and 16.5%, respectively, caused by RCM are listed in Tab. 5 exemplarily for two satellites.

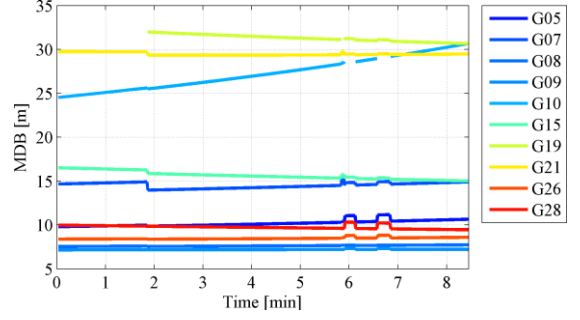


Fig. 24: Internal reliability (MDB: minimal detectable bias) of GPS satellites observed by receiver connected to Symmetricom CSAC w/o receiver clock modeling.

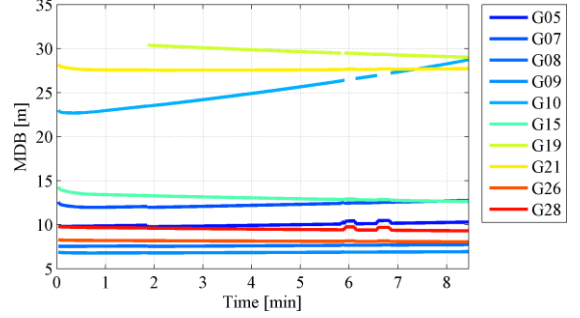


Fig. 25: Internal reliability (MDB: minimal detectable bias) of GPS satellites observed by receiver connected to Symmetricom CSAC with receiver clock modeling.

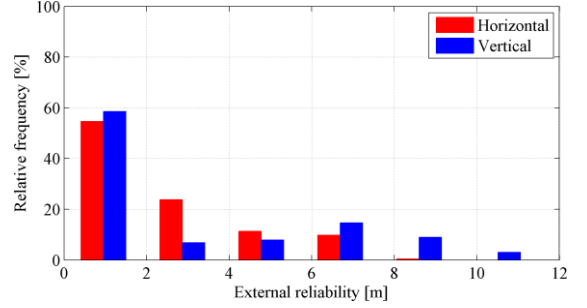


Fig. 26: Relative frequency of coordinates' external reliability $\nabla \mathbf{x}_i$ of receiver connected to Symmetricom CSAC w/o receiver clock modeling.

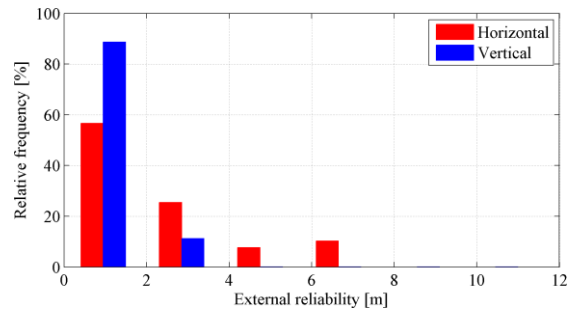


Fig. 27: Relative frequency of coordinates' external reliability $\nabla \mathbf{x}_i$ of receiver connected to Symmetricom CSAC with receiver clock modeling.

Tab. 5: Minimal and maximal improvements in (geometry-dependent) internal reliability for receiver connected to Symmetricom CSAC, exemplarily shown by two GPS satellites.

	G08	G15
Mean $\nabla \mathbf{z}_i$ w/o RCM [m]	7.62	15.64
Mean $\nabla \mathbf{z}_i$ w/RCM [m]	7.61	13.07
Improvement [%]	0.1	16.5

Due to the fact that MDB values are strongly dependent on the respective observation geometry no generally valid assumptions can be derived about the relationship between satellite position (elevation angle, azimuth) and improvements in internal reliability. In order to examine the impact of RCM on external reliability the coordinate's part of $\nabla \mathbf{x}_i$ derived from (5) are computed w/o and w/RCM, respectively, and divided into horizontal and vertical components. The relative frequencies of these values are depicted in Fig. 26 and Fig. 27.

It is clearly visible that there are almost no changes in the horizontal external reliability. The majority (57%) of these values remains below 2 m. However, in case of vertical external reliability a strong increase from 59% to 89% of values below 2 m occur when RCM is applied. Furthermore, almost no values bigger than 4 m remain. In contrast, w/o RCM approx. 35% of the vertical $\nabla \mathbf{x}_i$ values occur in the range between 4 m and 12 m.

CONCLUSIONS

An individual frequency stability characterization of three miniaturized atomic clocks was carried out w.r.t. the phase of an active hydrogen maser. In principle, the resulting Allan deviations show good agreement with manufacturer's data although both CSAC devices differ more or less significantly from the individual values.

Deriving PSD coefficients from the aforementioned ADEV values enables physically meaningful receiver clock modeling in GNSS applications. These individual coefficients were used in an Extended Kalman Filter to determine the clock process noise in true kinematic code-based GNSS single point positioning. In this way the up-coordinates' and up-velocities' precision could be improved up to 58% and 66%, respectively.

Furthermore, internal and external reliability were improved making the positioning solution much more robust against gross observation errors.

ACKNOWLEDGMENTS

The authors would like to thank Andreas Bauch and Thomas Polewka—who are both with PTB—for their support and commitment during execution and analysis of the clock comparisons.

We also thank IGS, CODE and ESOC for their free to use GNSS products which were a valuable contribution to our case study.

This work was funded by the Federal Ministry of Economics and Technology of Germany, following a resolution of the German Bundestag.

DISCLAIMER

The authors do not attempt to recommend any of the instruments under test. It is also to be noted that the performance of the equipment presented in this paper depends on the particular environment and the individual instruments in use. Other instruments of the same type or the same manufacturer may show different behavior.

However, the reader is encouraged to test his own equipment to identify the system performance with respect to a particular application.

REFERENCES

- [1] J. Dow, R. Neilan and C. Rizos, "The International GNSS Service in a changing landscape of Global Navigation Satellite Systems," *Journal of Geodesy*, vol. 83, pp. 191-198, 2009.
- [2] M. Rothacher and G. Beutler, "The role of GPS in the study of global change," *Physics and Chemistry of the Earth*, vol. 23, no. 9-10, pp. 1029-1040, 1998.
- [3] U. Weinbach, "Feasibility and impact of receiver clock modeling in precise GPS data analysis," no. 303, September 2012.
- [4] D. Allan, "Time and Frequency (The-Domain) Characterization, Estimation, and Prediction of Precision Clocks and Oscillators," vol. 34, pp. 647-654, 1987.
- [5] T. Krawinkel and S. Schön, "Application of Miniaturized Atomic Clocks in Kinematic GNSS Single Point Positioning," in *Proceedings of the 28th European Frequency and Time Forum*, Neuchatel, CH, 2014.
- [6] W. Riley, Handbook of Frequency Stability Analysis, NIST special publication 1065, 2008.
- [7] J. Barnes, A. Chi, L. Cutler, D. Healey, D. Leeson, T. McGunigal, J. Mullen, W. Smith, R. Sydnor, R. Vessot and G. Winkler, "Characterization of Frequency Stability," *IEEE Transactions on Instrumentation and Measurement*, vol. 20, pp. 105-120, 1971.
- [8] J. Zumberge, M. Heflin, D. Jefferson, M. Watkins and F. Webb, "Precise point positioning for the efficient and robust analysis of GPS data from large networks," *Journal of Geophysical Research*, vol. 102, pp. 5005-5017, 1997.
- [9] R. Dach, U. Hugentobler, P. Fridez und M. Meindl, Bernese GPS Software Version 5.0, Astronomical Institute, University of Bern, 2007.
- [10] J. Boehm, B. Werl and H. Schuh, "Troposphere mapping functions for GPS and very long baseline interferometry from European Centre for Medium-Range Weather Forecasts operational analysis data," *Journal of Geophysical Research*, vol. 111, 2006.
- [11] T. van Dam and R. Ray, "S1 and S2 Atmospheric Tide Loading Effects for Geodetic Applications," [Online]. Available: <http://geophy.uni.lu/ggfc-atmosphere/tide-loading-calculator.html>. [Accessed 7 May 2014].
- [12] H.-G. Scherneck, "Free ocean tide loading provider," [Online]. Available: <http://holt.oso.chalmers.se/loading/index.html>. [Accessed 7 May 2014].
- [13] A. van Dierendonck, J. McGraw and R. Grover Brown, "Relationship Between Allan Variances and Kalman Filter Parameters," in *Proceedings of the Sixteenth Annual Precise Time and Time Interval (PTTI) Applications and Planning Meeting*, Greenbelt, MD, 1985, pp. 273-292.
- [14] S. Schaer, W. Gurtner and J. Feltens, "IONEX: The IONosphere Map EXchange Format Version 1," in *Proceedings of the IGS AC Workshop, Darmstadt, Germany*, 1998.
- [15] M. Salzmann, "Least Squares Filtering and Testing for Geodetic Navigation Applications," *Netherlands Geodetic Commission, Publications on Geodesy*, no. 37, 1993.